# Nanomorphology-Enhanced Gas-Evolution Intensifies CO_2 Reduction Electrochemistry

Thomas Burdyny,[†] Percival J. Graham,[†] Yuanjie Pang,[†] Cao-Thang Dinh,[‡] Min Liu,[‡] Edward H. Sargent,[‡] and David Sinton*,[†]

[†]Department of Mechanical and Industrial Engineering, University of Toronto, 5 King's College Road, Toronto, ON Canada, M5S 3G8

[‡]Department of Electrical and Computer Engineering, University of Toronto, 10 King's College Road, Toronto, Ontario Canada, M5S 3G4

Ⓢ *Supporting Information*

ABSTRACT: Nanostructured CO_2 reduction catalysts now achieve near-unity reaction selectivity at increasingly improved Tafel slopes and low overpotentials. With excellent surface reaction kinetics, these catalysts encounter CO_2 mass transport limitations at current densities ca. 20 mA cm^{-2}. We show here that — in addition to influencing reaction rates and local reactant concentration — the morphology of nanostructured electrodes enhances long-range CO_2 transport via their influence on gas-evolution. Sharper needle morphologies can nucleate and release bubbles as small as 20 μm, leading to a 4-fold increase in the limiting current density compared to a nanoparticle-based catalyst alone. By extending this observation into a diffusion model that accounts for bubble-induced mass transport near the electrode's surface, diffusive transport can be

directly linked to current densities and operating conditions, identifying efficient routes to >100 mA cm^{-2} production. We further extend this model to study the influence of mass transport on achieving simultaneously high selectivity and current density of C2 reduction products, identifying precise control of the local fluid environment as a crucial step necessary for producing C2 over C1 products.

KEYWORDS: *Nanomorphology, CO_2 reduction, Gas-evolution, Limiting current, Electrocatalysis, Mass transport*
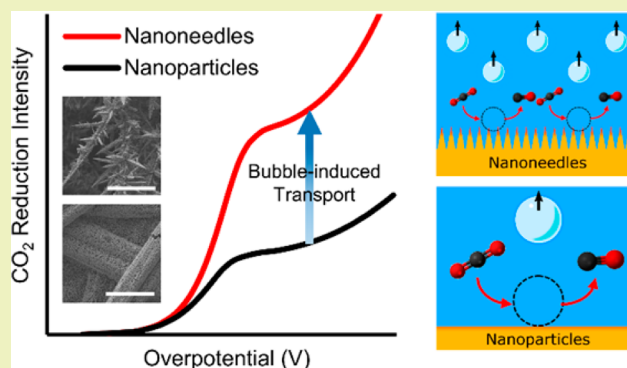
■ INTRODUCTION

The electrochemical conversion of CO_2 into fuels, both gaseous and liquid, is an emerging approach to mitigate fossil fuel based carbon emissions. Competing reactions, poor surface binding energies, low reactant solubility, and electrode stability all limit system performance and are major obstacles preventing electrochemical CO_2 reduction from widespread adoption.[1−4] To advance the field two distinct approaches have been adopted in the literature: 1) improving electrode kinetics, for instance through nanostructured electrodes with low activation potentials, high selectivity and high Tafel slopes, and 2) improving mass transport, such as increasing long-range CO_2 flux using pressurization, flow, or gas diffusion electrodes.[5,6] The field has advanced greatly in improving reaction kinetics, while further gains remain available in understanding and improving CO_2 transport to electrodes. Additionally, as electrocatalytic kinetics improve, transport limitations become more significant and ultimately limit performance.

Recent electrocatalysts for the CO_2 reduction reaction (CO_2RR) report high Tafel slopes and lower activation overpotentials when converting CO_2 into CO, HCOOH, and

multicarbon products. In each case performance advancements are attributed to engineered surface mechanisms. These strategies range from high energy surface structures that improve CO_2 surface binding energies;[7,8] oxide-derived materials that preferentially bind CO_2/CO;[9−11] and sharp morphologies resulting in field-induced reagent concentration.[12] As current is increased, however, the overpotential needed to further boost current density steadily increases due to pH gradients formed at the electrode and a decrease in the local concentration of CO_2.[13,14] At even higher currents, the CO_2 concentration at the electrode becomes depleted due to both consumption of CO_2 in the electrochemical reaction and unfavorable local pH conditions, limiting the maximum current density of CO_2 conversion. This limit cannot be overcome via CO_2 electrokinetics at the electrode surface. Increasing system pressure[5,15] and fluid flow[16] via devices is often quoted as a means to improve current density and selectivity in state-of-the-

art electrodes. Understanding the mass transport dynamics at play in experimental systems is essential, however, due to the direct influence of mass transport on observed catalyst performance. As an example the limiting current density of state-of-the-art electrodes has been experimentally shown to be enhanced by different surface morphologies (e.g., ~5 mA cm^{-2} for a flat Ag metallic surface,[17] ~15 mA cm^{-2} for Au-oxide nanoparticles,[9] ~55 mA cm^{-2} for Au nanoneedles[12]). Additionally, Rosen et al. reported a shift in the limiting current from ~10 mA cm^{-2} to ~35 mA cm^{-2} when switching from Ag nanoparticles to a nanoporous Ag structure under the same testing conditions.[18] These differences imply a significant impact of the electrode surface itself on the flux of CO_2 from the bulk to the electrode, although the exact mechanisms are unclear. There is a need to better understand the complex interactions between the catalyst and the surrounding fluid such that experimental results can be better interpreted, and, more importantly, future CO_2 reduction systems can be designed to reach higher currents.

To gain a more in-depth understanding of catalyst/electrolyte interactions several studies have investigated the dynamics of CO_2 and ion concentrations within a prescribed fluid diffusion layer at an electrode surface (~10−1000 μm).[14,19−22] These studies allowed for the performance impacts of pH and CO_2 gradients, electrolyte concentration, and temperature to be explored, identifying that significant overpotential losses and CO_2 depletion occur at relatively low current densities. The diffusion thickness which controls the limiting current density, however, is assumed to be a fixed value independent of operating conditions and electrode morphology. In parallel, other efforts have shown that mass transport due to gas-evolution is a primary driver of the diffusion thickness with transport increasing with current density and bubble release frequency.[23−26] Hydrogen evolution applications have subsequently utilized gas-evolution and electrode morphology to increase the physical stability of electrodes by reducing the residence time of formed hydrogen bubbles[27] while also increasing efficiencies by increasing active area and reducing ohmic drops and hysteresis at larger currents.[28−31] Applying these lessons to CO_2 reduction applications, the morphology of a CO_2 reduction catalyst can be similarly manipulated to enhance gas-evolution mass transport and increase the maximum intensity of CO_2 reduction electrochemistry. By combining existing CO_2 electrochemical models with gas-evolution theory and experimental observations a more complete model can be developed which accounts for the interconnected factors governing CO_2 reduction, illuminating existing and future experimental results.

In short, rapid recent advancements in catalyst performance coupled with low CO_2 solubility demand that transport limitations within CO_2 reduction systems be better understood and addressed. Herein we combine experimental observations with a mathematical model to quantify the role that catalyst nanomorphology plays in significantly enhancing mass transport for CO_2 reduction to CO and increasing the intensity at which the reaction can occur. Experimentally we visualize gas-evolution on established electrocatalyst electrode morphologies − nanoneedles, nanorods, and nanoparticles − and use the resulting observations to obtain a volume-averaged gas-evolution diameter for the surface. Combined with an electrochemical model accounting for mass transport from gas-evolution we compare our predicted findings with experimental results from Au nanoneedles and a similarly selective nanoparticle catalyst, emphasizing the influence of morphology-enhanced gas-evolution on the limiting current of experimental systems. Using this new perspective we discuss the impacts of electrode kinetics and CO_2 availability on product selectivity and partial currents as operating currents are varied. Finally, we extend our new interpretation of CO_2 reduction modeling to multicarbon (C2) products to identify existing mass transport limited performance and suggest an alternative experimental approach for achieving both high ethylene selectivity and low current densities on a copper catalyst.

■ MODELING SECTION

To model the performance of an electrochemical CO_2 reduction reaction it is necessary to take into account the combined effects of the electrode kinetics of the catalyst and the catalyst's interaction with the electrolyte. The electrode kinetics are modeled using the Butler−Volmer equation and experimentally obtained parameters for CO_2 reduction and hydrogen evolution (see the Supporting Information). The electrolyte/catalyst interactions are modeled as a 1-D diffusion system as discussed in the following sections.

Calculation of the Diffusion Thickness. As reactants (both CO_2 and H^+) are consumed at a catalyst's surface during an electrochemical reaction the concentration of molecules in the electrolyte will vary from that of the bulk. The concentration gradient is characterized by a diffusion layer adjacent to the electrode whose thickness directly correlates to the reaction's limiting current density and polarization losses. In previous electrochemical models for CO_2 reduction the diffusion layer thickness is prescribed as a specific value independent of current density or electrode morphology. Here we approximate the thickness of the diffusion layer as a function of operating parameters, allowing it to vary with current density.

In a 1-D planar system the thickness of the diffusion layer is equal to the diffusivity of the species of interest, D_i, divided by the mass transfer coefficient, k_m, present in the system:

$$\delta_i = \frac{D_i}{k_m} \tag{1}$$

The mass transfer coefficient can be found by accounting for the combined effects of the two primary mass transfer mechanisms present in the system: convective bulk flow and bubble-induced momentum from gas-evolution.

$$k_m = k_{conv} + k_{bubble} \tag{2}$$

Mass transfer effects for convective flow can be found using the well-known correlation for flow over a flat plate where the average mass transfer coefficient calculated from the Sherwood number is

$$k_{conv} = \frac{\overline{Sh}D_i}{L} = \frac{0.664D_i}{L}Re_L^{0.5}Sc^{0.333} \tag{3}$$

where the characteristic length, L, is the length of the electrode in direction of flow. The Reynolds number can be approximated from the stirring or flow conditions of the electrolyte.

For gas-evolution, several mechanisms contribute to the replenishment of reactant at the electrode surface including bubble growth, break-off, and wake flow. A number of numerical correlations have been created to describe these

mass transfer processes using a combined mathematical and empirical approach. Collectively, however, these correlations are in relative agreement as described by Vogt et al.[23,24] To describe the effects of bubble break-off where fluid immediately replaces the departing bubble, Sh_1, we use the Roušar correlation,[32,33] and to describe the combined effects of bubble growth and wake flow, Sh_2, we use Vogt's correlation for low electrode bubble coverage $(\Theta < 0.5)$[24]

$$Sh_1 = \sqrt{\frac{12}{\pi}} Re_G^{0.5} Sc^{0.5} \Theta^{0.5} \tag{4}$$

$$Sh_2 = \frac{2}{\sqrt{5}} Re_G^{0.5} Sc^{0.34} \left(1 - \frac{\sqrt{8}}{3}\frac{R_a}{R}\Theta^{0.5}\right)(1 + \Theta) \tag{5}$$

where Θ represents the fraction of the electrode area shielded by bubbles during a bubble's residence time and thus not available for reactions. The ratio R_a/R in eq 5 represents the ratio of inactive electrode area below a nucleated bubble as it grows. The Reynolds and Schmidt numbers for gas-evolution are described as

$$Re_G = \frac{\dot{V}_{gas}}{A}\frac{d_b}{v} \tag{6}$$

$$Sc = \frac{v}{D} \tag{7}$$

For gas-evolution the bubble departure diameter, d_b, acts as the characteristic length scale, while v is the kinematic viscosity of the electrolyte. The volume flux from gas-evolution $(\dot{V}_{gas}/A)$ represents the effective gas velocity and is defined as

$$\frac{\dot{V}_{gas}}{A} = \frac{j_{evolved}}{n_e F}\frac{RT}{P} \tag{8}$$

where pressure, P, and temperature, T, are generally known during experiments, and the gas-evolving current, $j_{evolved}$, is the sum of all currents which form products that depart in the gaseous phase.

As described by Vogt the mass transport effects from bubble break-off, and growth/wake flow occur simultaneously and compete with one another. These can thus be combined into a single Sherwood number from which the overall mass transfer coefficient from gas-evolution can be extracted:

$$Sh_{bubble} = (Sh_1^2 + Sh_2^2)^{0.5} \tag{9}$$
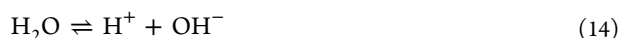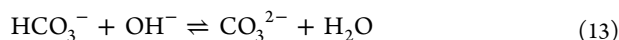
$$k_{bubble} = \frac{Sh_{bubble} D_i}{d_b} \tag{10}$$

For our analysis we assume that the bubble coverage, Θ, is a constant 25%, while R_a/R is assumed to be 0.75.[24] It is worth noting that the mathematically derived Sherwood numbers in eq 4 and 5 assumed a flat electrode and a bubble contact angle of 90°. As nanostructured electrodes have a much higher electrochemically active surface area and are generally hydrophilic, the mass transfer coefficient calculated here is conservative, underpredicting most CO_2 reduction electrodes due to the reduced fraction of inactive surface where bubbles contact the electrode surface.

From eqs 1–10 the thickness of the diffusion layer can be calculated as a function of the gas-evolving current density, bubble departure diameter, pressure, and fluid flow velocity. The bubble departure diameter is an experimentally determined

quantity which depends upon the morphology and wettability of a catalyst's surface.

Numerical Modeling of the Diffusion Layer. With the diffusion layer thickness calculated as a function of operating conditions, the concentrations of reactants within the diffusion layer can be approximated using the Nernst−Planck equation.[14,20,22] Here we utilize a similar approach to Gupta et al. assuming that the bulk electrolyte remains saturated with CO_2 during the reaction and the effects of migration are negligible.

We first account for the chemical equilibrium formed between CO_2, HCO_3^-, CO_3^{2-}, OH^-, and H^+ in an aqueous solution governed by the following equations

$$CO_{2(aq)} \rightleftharpoons CO_{2(g)} \tag{11}$$

$$CO_{2(aq)} + OH^- \rightleftharpoons HCO_3^- \tag{12}$$

$$HCO_3^- + OH^- \rightleftharpoons CO_3^{2-} + H_2O \tag{13}$$

$$H_2O \rightleftharpoons H^+ + OH^- \tag{14}$$

whose respective equilibrium constants K_0, K_1, K_2, and K_w are determined as functions of temperature and salinity as described in the Supporting Information. From these equations the bulk concentrations of each component can be found for different electrolyte concentrations, temperatures, and operating pressures. The "salting out" effect of CO_2 due to the addition of $NaHCO_3$ and $KHCO_3$ is also accounted for as described by eqs S5−S7.

Conservation of mass can then be applied within the diffusion layer bounded by the catalyst surface $(x = 0)$ and the bulk electrolyte $(x = \delta)$ resulting in the following governing equations[22]

$$\frac{\partial[CO_2]}{\partial t} = D_{CO_2}\frac{\partial^2[CO_2]}{\partial x^2} - [CO_2][OH^-]k_{1f} + [HCO_3^-]k_{1r} \tag{15}$$

$$\frac{\partial[HCO_3^-]}{\partial t} = D_{HCO_3^-}\frac{\partial^2[HCO_3^-]}{\partial x^2} + [CO_2][OH^-]k_{1f} - [HCO_3^-]k_{1r} - [HCO_3^-][OH^-]k_{2f} + [CO_3^{2-}]k_{2r} \tag{16}$$

$$\frac{\partial[CO_3^{2-}]}{\partial t} = D_{CO_3^{2-}}\frac{\partial^2[CO_3^{2-}]}{\partial x^2} + [HCO_3^-][OH^-]k_{2f} - [CO_3^{2-}]k_{2r} \tag{17}$$

$$\frac{\partial[OH^-]}{\partial t} = D_{OH^-}\frac{\partial^2[OH^-]}{\partial x^2} - [CO_2][OH^-]k_{1f} + [HCO_3^-]k_{1r} - [HCO_3^-][OH^-]k_{2f} + [CO_3^{2-}]k_{2r} \tag{18}$$

with the diffusion coefficients, D_i, and equilibrium rate constants $(k_{1f}, k_{1r}, k_{2f}, k_{2r})$ found in the Supporting Information. At the catalyst surface the flux of CO_2 and OH^- are proportional to the CO_2 reduction current density and total current density, respectively. At the edge of the Nernst diffusion layer the concentrations of each species equal the bulk concentrations as determined from the equilibrium expressions in eqs 11−14. The concentration of each species in the diffusion layer can then be solved by prescribing a current density and Faradaic efficiency.

Modeling Electrochemical CO_2 Reduction. From the steady-state concentrations of CO_2 and OH^- at the catalyst
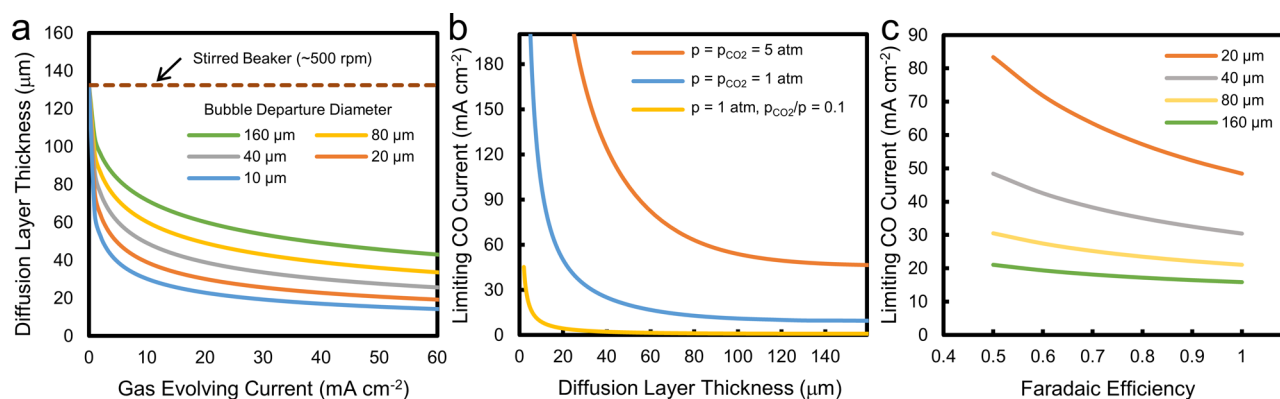
Figure 1. Impact of operating conditions on the maximum performance of gas-evolving CO_2 reduction systems. a) Effect of various monodisperse bubble departure diameters on diffusion layer thickness at $P = 1$ atm, b) effect of diffusion thickness on the CO limiting current density at 100% CO selectivity for various total and partial pressures (0.5 M $KHCO_3$ electrolyte), and c) effect of Faradaic efficiency and hydrogen evolution on the limiting current density in CO production on Au catalysts.

surface found using eqs 11−18 the polarization overpotentials resulting from pH gradients and the depletion of CO_2 reactant are postcalculated as follows

$$\phi_{pH} = \frac{2.303RT}{F}(\log([OH^-])_{x=\delta} - \log([OH^-]_{x=0})) \tag{19}$$

$$\phi_{CO_2} = \frac{RT}{nF} \log\left(\frac{[CO_2]_{x=\delta}}{[CO_2]_{x=0}}\right) \tag{20}$$

where R is the universal gas constant, F is Faraday's constant, and n is the number of electrons required for the CO_2 reduction reaction. On the gold catalyst used in this paper only CO_2 reduction to CO and hydrogen evolution are assumed to take place which are both two electron processes:

$$2H_2O + 2e^- \rightarrow H_2 + 2OH^- \tag{21}$$

$$CO_{2(aq)} + H_2O + 2e^- \rightarrow CO + 2OH^- \tag{22}$$

The overpotential losses can then be added to the previously obtained Butler−Volmer curves for CO_2 reduction to CO and hydrogen evolution to predict the voltage vs current curve for the cathodic reaction.

During the reaction both CO and H_2 evolution are present with both contributing to the evolved gas in eq 8 and subsequently the diffusion thickness and polarization losses. Modeling the electrochemical reaction from the Tafel curves without prescribing a Faradaic efficiency then requires an iterative process as the polarization losses are postcalculated and the effects of CO_2 depletion only affect the CO evolution reaction. To that end an initial Faradaic efficiency is assumed, and the simulation is run to gain an initial estimation of the polarization losses. From the resulting overpotentials a new Faradaic efficiency is calculated, and the simulation is rerun until the iterated value converges. At convergence the applied electrode potentials for CO_2 reduction and H_2 evolution are equal, and the partial current densities sum to the prescribed total. Finally, the limiting current density for CO_2RR is determined to be the effective current density where the concentration of CO_2 at the electrode surface is equal to the rate at which it is generated by bicarbonate equilibrium.

■ RESULTS AND DISCUSSION

Influence of Gas-Evolution on Mass Transport and CO_2 Reduction Intensity. Mass transport in electrochemical CO_2 reduction systems is imperative given the low solubility of CO_2 in aqueous systems and the large increase in currents needed to reach industrially relevant currents. Within aqueous electrochemical systems gas-evolution is known to be a primary driver of transport but depends on factors such as current density, bubble dynamics, and wettability among others. Here we utilize mass transfer relations for gas-evolution and convective flow to estimate an effective diffusion layer thickness (Nernst diffusion layer) which can be used in a broader electrochemical CO_2 reduction model for predicting CO_2 reduction performance.

Using eqs 1−10 we calculate the expected diffusion thickness for various monodisperse bubble departure diameters and currents from gas products (gas-evolving currents) as seen in Figure 1a. Since most aqueous systems are stirred, the approximated diffusion layer for a stirred beaker at ~500 rpm is also shown[34] assuming a local flow velocity of 1 cm s^{-1} and electrode width of 0.5 cm. Figure 1a implies that the effective mass transport at the electrode due to bubble growth and departure is much greater than a moderately stirred beaker, particularly at current densities >10 mA cm^{-2} where the diffusion thickness for even large bubbles is half that of a stirred beaker alone. As departure diameter is decreased the number and frequency of bubbles on a catalyst's surface increase resulting in a boost in mass transport. An increase in the gas-evolving current further decreases the diffusion thickness as observed experimentally elsewhere.[35,36] Previous CO_2 reduction models[14,19−22] have utilized a fixed diffusion layer rather than accounting for the large variability that occurs as current density and bubble departure diameters are altered.

The effects of altering the bulk CO_2 concentration are observed in Figure 1b by varying the total and partial pressure of CO_2 assuming an electrode selectivity of 100% toward CO. While all three curves are proportional, the absolute current densities are very different owing to the increased dissolved CO_2 at higher pressures. Observing the 1 atm curve we can see that overcoming the commonly seen limiting currents of ~20 mA cm^{-2} requires diffusion thicknesses of less than 50 μm. Reaching these thicknesses would then require either a significant increase in forced convection or enhanced product release from the catalyst surface. Figure 1b also shows that
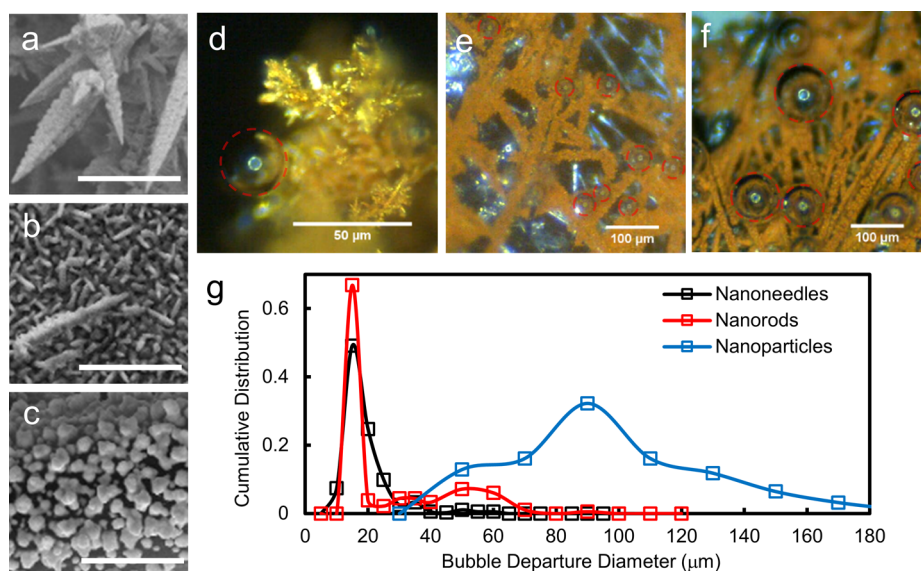
Figure 2. SEM images of a) nanoneedles, b) nanorods, and c) nanoparticles (inset scale bars are 5 μm). Influence of electrode morphology on bubble departure sizes for d) nanoneedles, e) nanorods, and f) nanoparticles, see Supporting Information videos, and g) cumulative distribution curve of bubble release diameters for Au electrodes with nanoneedle, nanorod, and nanoparticle morphologies.

pressure and mass transport have an additive effect on CO_2 availability and hence the maximum CO_2 reduction intensity while highlighting the need for pure CO_2 inputs even in high mass transport cases.

Given the importance of selectivity on performance, the impacts of Faradaic efficiency are also analyzed for a catalyst capable of producing CO and H_2. As shown in Figure 1c as H_2 evolution is increased the maximum intensity for CO production subsequently increases following from the increase in evolved gases. The relative impact of bubble diameters also indicates that only small bubbles diameters are expected to greatly increase the absolute CO_2 reaction intensity.

Although mass transport from gas-evolution has been studied both experimentally and numerically, several limitations exist when applying the derived relations to experimental catalysts. For instance the Sherwood numbers in eqs 4 and 5 generally assume a horizontal, flat electrode in a stagnant reactor. Directionality and convective flow both effect gas-evolution dynamics, but variations versus stagnant conditions are generally considered minimal in low flow conditions (<0.1 m s^{-1}) versus the overall transport mechanism.[36,37] Electrode bubble coverage is another assumption which factors into both the derivation and use of eqs 4 and 5 and varies between 0.1 and 0.3 for the current densities of interest.[38] While mass transport from gas-evolution is greatly reduced for lower values of bubble coverage, Vogt found the approximation to underpredict experimental findings as bubble coverage tends toward zero. These combined factors reflect some uncertainty, but the overall calculated magnitude of the mass transfer coefficient remains similar to that predicted in Figure 1 for various operating conditions.

Nanomorphology-Enhanced Mass Transport. Nanomorphology has been effective in improving electrode kinetics and reducing the overpotentials needed to convert CO_2 at low currents via a number of surface based approaches. To maintain record efficiency and selectivity at higher currents, however, the long-range flux of CO_2 to the electrode must be increased. As the reduction of CO_2 into CO necessarily results in gas-evolution − which in turn promotes dissolved CO_2 flux −

enhancement of this phenomenon by manipulating nano-morphology provides a secondary means for the catalyst surface to influence reaction rates.

To assess the influence of nanomorphology on mass transport we first visualized CO gas-evolution using a dark field microscope for three different electrode morphologies shown in Figure 2a-c: Au nanoneedles, nanorods, and nanoparticles. The nanoneedles had a noticeably smaller bubble departure diameter with a mean diameter of 23 μm based upon the volume-averaged bubble diameter (Figure 2d and Supporting Information video). Under otherwise similar conditions, bubbles on the nanorod and nanoparticle surfaces had average release diameters of 31 and 97 μm, respectively (Supporting Information videos). In the case of nanoneedles and nanorods a large number of small bubble trains emanated from the surface with some larger bubbles seen in the nanorod case which increased the overall diameter. For the nano-particles, however, bubbles resided on the surface for much longer times allowing for growth via diffusion. Exposed carbon paper in areas where the catalyst was removed showed the greatest bubble release diameters as expected from the reduced wettability versus gold. Through their structure, nanoneedles reduce the bubble contact diameter decreasing the forces adhering it to the surface, and the increased agitation promotes bubble detachment. The effervescent generation of small bubbles from the nanoneedles (Figure 2) provides improved transport as quantified by the small diffusion thickness (Figure 1) and intensified CO_2 reduction. While the volume-averaged bubble diameter can be used in eqs 4−10 to calculate an effective diffusion layer thickness, it is accurate only for monodisperse or narrow bubble distribution. For bimodal or polydisperse distributions a collective mass transfer coefficient should instead be calculated using a weighted average of the mass transfer coefficients of bubble subpopulations. As detailed in the Supporting Information, including measured bubble size distributions resulted in variations of only 5% in terms of diffusion thickness for nanoneedles and particles (details in the Supporting Information).

Using our varying-diffusion-layer electrochemical model (eqs 1−22), we predict the performance of Au nanoneedles and a similarly selective nanoparticle CO_2RR catalyst with a flatter morphology. We chose Au-oxide nanoparticles[9] as an appropriate fair point of comparison due to the similar product, high selectivity, good Tafel slope, and defined microstructure. The electrode kinetics of each morphology are separated from transport related effects by using the experimentally determined Tafel slopes and exchange current densities (see the Supporting Information). Inputting the system operating conditions into our 1D model, we can then simulate the expected over-potentials and polarization losses for a range of current densities and average bubble size in the system (see Modeling Section for details). The Faradaic efficiency of CO and H_2 evolution are calculated in the model by accounting for the combined effects of the electrode kinetics, electrolyte conditions, and polarization losses. Figure 3a and b show the predicted CO partial current density versus overpotential for three different bubble departure diameters with the exper-imental results overlaid. Also included is the CO evolution Tafel curve (no losses) for reference. For the Au-oxide nanoparticles an inputted mean bubble diameter of 100 μm
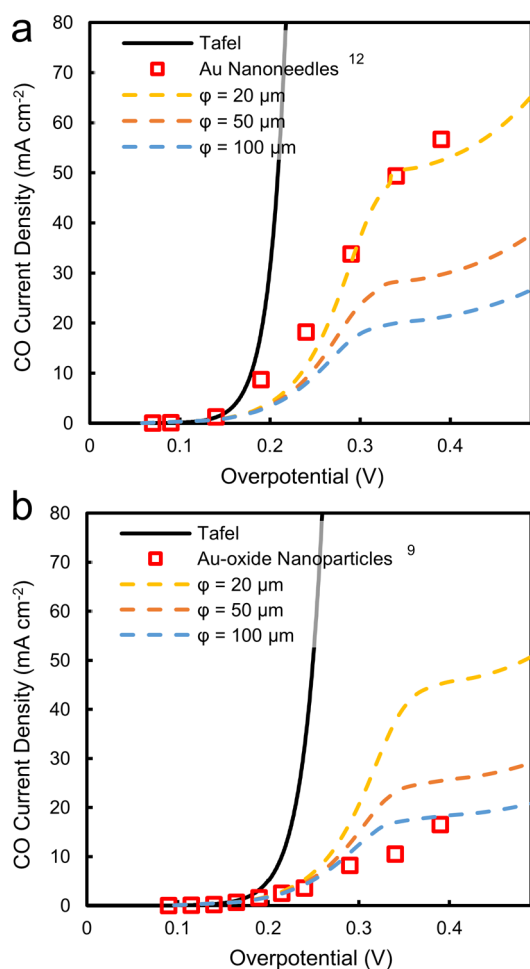

in our simulation best matched the experimental limiting current density of 15 mA cm^{-2}, comparing well with our experimentally observed bubble diameters on Au nanoparticles (Figure 2d) and similar to that reported elsewhere on a Pt catalyst.[30] For nanoneedles, the curve simulated using a 20 μm bubble diameter was needed to boost the limiting current to >50 mA cm^{-2}, giving a similar result to the observed bubble diameter from Figure 2d. In both cases the partial CO current slowly increases after temporarily plateauing as hydrogen evolution provides the further mass transport needed to supply additional CO_2 (see Figure 2d). Together, these results show the importance of morphology-dependent gas-evolution dynamics on experimental CO_2 reduction performance and their importance in modeling electrochemical systems.

In Figure 4 we illustrate how electrode nanomorphology can increase long-range transport by influencing gas-evolution, resulting in a 4-fold increase in limiting current density of CO production for nanoneedles over nanoparticles. Similar to what has been found in heat transfer analyses along a surface,[39] the enhanced mass transport stems from a reduction in the departure diameter of bubbles from the electrode surface. Designing electrodes that provide this level of mixing can then be more efficient and potentially forego high-velocity forced fluid flow that would otherwise be necessary to provide sufficient CO_2 to a surface. Further pairing the above passive approach for increasing current density with a pressurized system a high current density and product purity system may also be possible as an alternative to gas diffusion electrodes which limit product purity in the effluent stream and have poorer catalyst flexibility.

From both Figure 3a and b it is also possible to see the effect that mass transport has on polarization losses in the system, particularly as the current approaches the limiting value. These losses become inevitable as CO_2 concentration decreases and supports the findings of Chen et al.[19] regarding the importance of operating electrochemical CO_2 reduction cells at 80−90% of their maximum current density. It is important to note that differences in electrode morphology in turn result in large differences in the overall electrochemically active surface area which impacts both electrode kinetics and the current density normalized by the active surface area.[12] In addressing the limiting CO2RR current density of the electrode, however, the geometric current density is of primary importance as the flux of CO_2 to the catalyst is dependent on the planar area of the electrode rather than the specific surface area of catalyst.

Further optimization of electrode morphology for mass transport purposes is also possible as exhibited by bubble trains as small as 10 μm in portions of the nanoneedle and nanorods electrodes (Figure 2d). Facilitating bubble departure could be accomplished, for instance, using a more organized needle structure or even including nonparticipating structures which promote bubble nucleation and detachment. Increasing electrode wettability would achieve a similar result, but changes to the surface would simultaneously impact electrode kinetics. Finally, adding a nonionic surfactant to the liquid at close to the critical micelle concentration can lower the surface tension of water from ∼72 mN m^{-1} closer to ∼33 mN m^{-1}, enough to aid in the release of bubbles from the surface at smaller diameters.[40−42] As confirmation, by adding 0.8 times the CMC of Triton X-100 to the electrolyte we were able to reduce the residence time of bubbles by over half with an average departure diameter from the catalyst surface of 40 μm (Figure
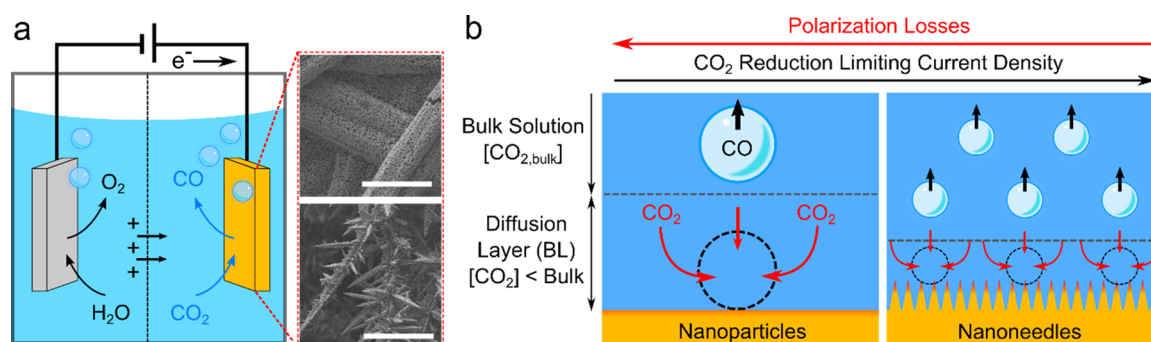
Figure 3. Comparison between predicted and experimental steady-state current versus voltage curves for assumed bubble departure diameters of 20, 50, and 100 μm highlighting the impact of morphology on limiting current density and polarization losses. a) Performance of Au nanoneedles[12] in 0.5 M KHCO$_3$ and b) performance of Au-oxide nanoparticles[9] in 0.5 M NaHCO$_3$.

Figure 4. a) Electrochemical cell for CO_2 reduction showing either a flatter or a sharper nanostructured electrode (scale bar is 20 μm). b) Schematic depicting the influence of electrode morphology on bubble departure diameter and the resulting thickness of the diffusion boundary layer. Fresh electrolyte fills the region previously occupied by nucleated bubbles on the electrode's surface.

S1 and Supporting Information video), indicating another route to higher CO_2 mass transport via gas evolution.

Effect of CO_2 Availability on CO_2 Reduction Selectivity. Selectivity toward specific CO_2 reduction products (CO, HCOOH, C_2H_4, etc.) over H_2 evolution has been the central subject of numerous theoretical[43−45] and experimental[46,47] works. These efforts explore direct conversion kinetics but leave out CO_2 availability as a driver of CO_2RR selectivity and the corresponding impact of mass transport as current increases.

Using nanoneedles, we identify the contributing factors of CO_2 availability toward selectivity. From the reported Tafel slope the ideal CO_2RR curve for the FIRC needles is shown in Figure 5a. Also using the experimental results, we extract the HER (Hydrogen Evolution Reaction) Tafel curve and plot within the same figure (see Modeling Section). Alongside these ideal curves are the predicted polarization losses from pH gradients and CO_2 depletion (denoted by ϕ) assuming a volume averaged bubble departure diameter of 20 μm. As current density increases these losses steadily increase proportional to the OH^- and CO_2 concentration at the electrode. It is important to note that the overpotential due to a pH gradient (ϕ_{pH}) at the electrode surface is a function of the total current density and affects both reaction products. The total and partial current densities for CO and H_2 are then plotted in Figure 5b next to experimental data. Finally the selectivity toward CO as well as the electrode CO_2 concentration for a range of overpotentials are plotted in Figure 5c, agreeing well with the Au needle experimental data.[12]

Three interesting conclusions can be made from the plots in Figure 5. First, as long as the Tafel slope of CO_2RR is greater than that of HER and the activation overpotential is lower, the high Faradaic efficiency of CO production is maintained provided ample CO_2 is supplied to the electrode. Concentration polarization losses are then kept small until ~45 mA cm^{-2} where selectivity slowly begins to decrease. Second, as H_2 evolution increases at higher overpotentials the thickness of the diffusion layer continues to decrease due to additional gas generation and mass transport, as seen in Figure 1a and Figure S2. The partial current density of CO then sees a small rise at higher voltages instead of plateauing, albeit at lower FE. Without transport increasing with gas-evolution the absolute CO partial current would remain constant after the limiting current. Finally, the poor CO Faradaic efficiency below 0.2 V is the result of more favorable H_2 evolution even though H_2 evolution kinetics are worse at higher overpotentials (highlighted inset in Figure 5a). This widely seen trend is due to the

0.10 V lower activation potential for H_2 evolution ($E^o_{H_2}$ = 0 V versus $E^o_{CO_2}$ = −0.10 V RHE).

The analysis here can be applied to any mixture of gas and liquid CO_2RR products and can be used to determine losses and the limiting current density even when a large number of products are present (e.g., on a copper electrode). The greatest CO_2RR current densities will be seen at higher volumes and ratios of gas products as described by Figure 1a and b. Systems with purely liquid CO_2RR products have shown lower current densities than gaseous products (e.g. 5−10 mA cm^{-2} for formate), implying that performance suffers in the absence of bubble-induced transport.

High Intensity Production of C2 Products. Here we extend the experiment-validated idea of a variable diffusion layer and current-dependent mass transport to C2 reduction products in an effort to guide future experiments toward both high product selectivity and current density. To date both experimental and modeling efforts have shown the importance of a high local electrode pH on ethylene (C_2H_4) selectivity due to the pH-dependent pathway for methane production allowing for high Faradaic efficiencies to be achieved on copper electrodes using low buffering capacities (0.1 M) and increased system pressures.[48−50] Operating at too high a pH, however, shifts carbonate equilibrium away from CO_2.[14] As a consequence, while lower electrolyte buffering capacities result in high ethylene selectivities, the ethylene partial current is constrained at higher currents due to a shortage of CO_2. Rather than operating at a high local pH the local environment of the catalyst should be regulated to achieve both the desired ethylene selectivity and current density. In Figure 6 we briefly show the sensitivity of common operating conditions (buffering, pressure, mass transport) on the local pH and CO_2 availability versus a standard operating condition (0.1 M $KHCO_3$, 1 atm) using our model accounting for current dependent mass transport.

For simplicity we assume a Faradaic efficiency distribution of 40% ethylene, 40% hydrogen, and 20% liquid HCOOH in all cases though the exact ratio of methane/ethylene would change with current and pH. A bubble departure diameter of 100 μm is assumed to represent a typical electrode surface, while a baseline convective flow from stirring is also assumed as before (500 rpm, Figure 1a). The effects of buffering capacity and pressure on CO_2 solubility and carbonate equilibrium are again taken into account in the Supporting Information. Termination of a line indicates the point where no CO_2 is present at the catalyst surface which in all cases happened close to a pH of 12.
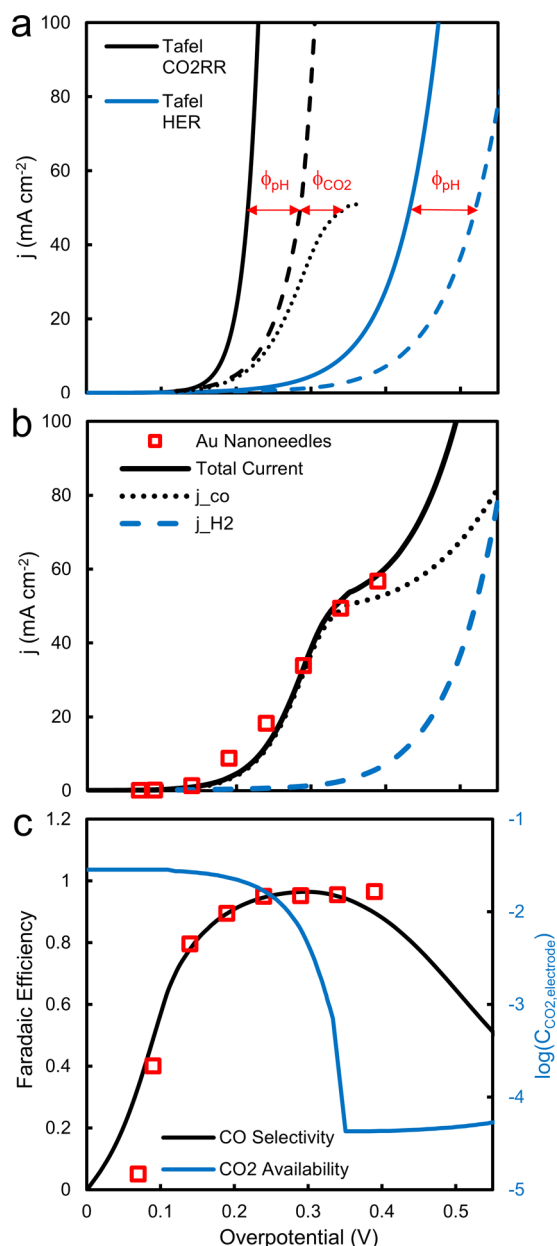
Figure 6. Local electrode pH as a function of current density for various electrolyte $KHCO_3$ concentrations, pressures, and bubble departure diameters. Selectivity fixed as 40% C_2H_4, 40% H_2, and 20% HCOOH. The termination of a line indicates that CO_2 has been fully depleted.

total currents, however, are possible as compared to the more weakly buffered case. When the electrolyte concentration is brought back to 0.1 M and the pressure increased to 3 atm, a similar initial trend exists as in the 1 atm case. Due to the increased CO_2 concentration at higher pressures, however, the system remains buffered and is allowed to reach total currents of over 65 mA cm^{-2} before depleting all available CO_2. It is worth noting that the increase in current over the 1 atm case is only 25 mA cm^{-2} showing the necessity of either further buffering or mass transport to ensure that the 3-fold larger initial CO_2 concentration is fully utilized for ethylene production. Finally we see that in the case of enhanced mass transport from a smaller bubble diameter of 20 μm, maximum currents of over 100 mA cm^{-2} are possible even at a low electrolyte concentrations. Each of the proposed approaches is a demonstration of how higher ethylene partial currents can be reached by preventing the local electrode pH from getting so high that CO_2 is lost to a shift in the carbonate equilibrium. Controlling pH with sufficient combinations of electrolyte, pressure, and mass transport then provides an avenue to both high ethylene selectivity and current density. These results highlight the importance of combining modeling and experimental efforts to ensure that the best operating and testing conditions are identified to maximize performance.

■ CONCLUSIONS

Widespread application of CO_2 reduction will necessitate high current densities and progress in both electrode kinetics and mass transport. These are linked by the low solubility of CO_2 in aqueous media and the importance of process conditions on measured performance. In addition to influencing reaction rates and local reactant concentration, we show that the morphology of nanostructured electrodes can also enhance long-range CO_2 transport via their influence on gas-evolution, effectively extending the reach of the nanostructure into solution. This is supported by an electrochemical model which deviates from previous CO_2RR efforts with the inclusion of bubble-induced mass transport via a variable diffusion layer thickness. This relatively straightforward approach replicated trends observed experimentally, most notably differences in limiting currents achieved with different electrode morphologies. A more complete understanding of the transport mechanisms affecting the selectivity and current densities of experimental electrodes and their results is then enabled as compared to previous works.

Figure 5. a) Butler−Volmer curves for CO_2RR and HER for gold nanoneedles with CO_2 saturated 0.5 $KHCO_3$. Inset shows more favorable HER kinetics at low overpotentials. Dashed lines indicate the addition of polarization overpotentials (ϕ) for a 20 μm bubble departure diameter. b) Partial and total simulated current densities. c) Selectivity and CO_2 availability of the catalyst for CO_2RR using the loss adjusted CO_2RR and HER curves in a). Red experimental data is from Au nanoneedles[12] in 0.5 M $KHCO_3$.

Observing the curves in Figure 6 the relative impacts of changing each operating condition on the maximum current density and pH can be seen. First, systems with low buffering capacity will reach high pH values at overall lower current densities allowing for higher ethylene/methane ratios to be produced at low currents. The penalty with this approach, however, is the CO_2 at the electrode being depleted at modest currents of ~40 mA cm^{-2}. The maximum ethylene partial current is then limited to less than 16 mA cm^{-2} as has been obtained experimentally.[48,49] As the buffer is increased to 0.2 M the current needed to reach higher local pH increases, implying that more methane will be produced at lower currents. Higher
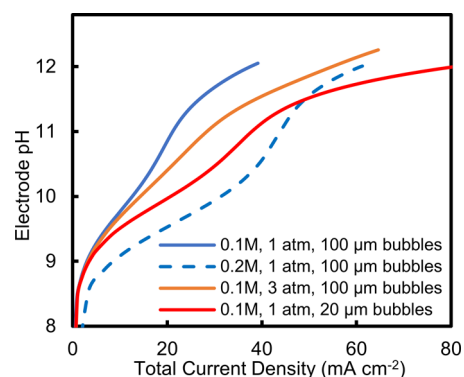
Application to gas, liquid, or combinations of products can help to guide experiments toward more promising operating conditions as well as interpreting existing results. The complexity of the model would need further enhancement for scenarios where factors such as surface poisoning affect product composition but could be incorporated into the underlying electrode kinetics. One instance of this involves CO surface poisoning which can either promote or delay hydrogen evolution at lower voltages.[51] Collectively, this work illustrates how electrode morphologies influence not only short-range reaction and concentration effects but also long-range CO_2 transport and provides a framework for quantifying the impacts of operating parameters and electrode kinetics on product selectivity and efficiency.

ASSOCIATED CONTENT

Supporting Information

The Supporting Information is available free of charge on the ACS Publications website at DOI: 10.1021/acssuschemeng.7b00023.

> Discussion of the modeling approach, experimental procedures for measuring bubble release diameters for different morphologies, supplementary modeling curves, and estimation of local electrode pH (PDF)
>
> Bubble departure video for a nanoneedle electrode morphology - 1 (AVI)
>
> Bubble departure video for a nanoneedle electrode morphology - 2 (AVI)
>
> Bubble departure video for a nanorod electrode morphology (AVI)
>
> Bubble departure video for a nanoparticle electrode morphology (AVI)
>
> Bubble departure video for a nanoparticle electrode morphology with surfactant in the electrolyte (AVI)

AUTHOR INFORMATION

Corresponding Author

*E-mail: sinton@mie.utoronto.ca.

ORCID

Thomas Burdyny: 0000-0001-8057-9558
David Sinton: 0000-0003-2714-6408

Author Contributions

T.B. proposed the idea developed in this work. T.B. performed the bubble capture experiments and analysis. T.B. and P.J.G. designed and performed simulation efforts. Y.P. and M.L. fabricated electrode morphologies and obtained SEM images. All authors contributed to the manuscript. D.S. and E.H.S. supervised this work.

Notes

The authors declare no competing financial interest.

ACKNOWLEDGMENTS

ABBREVIATIONS

CO2RR, CO_2 reduction reaction; HER, hydrogen evolution reaction; RHE, reversible hydrogen electrode

REFERENCES

(1) Kondratenko, E. V.; Mul, G.; Baltrusaitis, J.; Larrazábal, G. O.; Pérez-Ramírez, J. Status and perspectives of CO2 conversion into fuels and chemicals by catalytic, photocatalytic and electrocatalytic processes. *Energy Environ. Sci.* **2013**, *6* (11), 3112−3135.

(2) Lu, Q.; Jiao, F. Electrochemical CO2 reduction: Electrocatalyst, reaction mechanism, and process engineering. *Nano Energy* **2016**, *29*, 439−456.

(3) Jhong, H.-R. "Molly"; Ma, S.; Kenis, P. J. Electrochemical conversion of CO2 to useful chemicals: current status, remaining challenges, and future opportunities. *Curr. Opin. Chem. Eng.* **2013**, *2* (2), 191−199.

(4) Zhu, S.; Shao, M. Surface structure and composition effects on electrochemical reduction of carbon dioxide. *J. Solid State Electrochem.* **2016**, *20* (4), 861−873.

(5) Dufek, E. J.; Lister, T. E.; Stone, S. G.; McIlwain, M. E. Operation of a Pressurized System for Continuous Reduction of CO2. *J. Electrochem. Soc.* **2012**, *159* (9), F514−F517.

(6) Thorson, M. R.; Siil, K. I.; Kenis, P. J. A. Effect of Cations on the Electrochemical Conversion of CO2 to CO. *J. Electrochem. Soc.* **2013**, *160* (1), F69−F74.

(7) Wang, Z.; Yang, G.; Zhang, Z.; Jin, M.; Yin, Y. Selectivity on Etching: Creation of High-Energy Facets on Copper Nanocrystals for CO2 Electrochemical Reduction. *ACS Nano* **2016**, *10* (4), 4559−4564.

(8) Zhu, W.; Michalsky, R.; Metin, Ö.; Lv, H.; Guo, S.; Wright, C. J.; Sun, X.; Peterson, A. A.; Sun, S. Monodisperse Au Nanoparticles for Selective Electrocatalytic Reduction of CO2 to CO. *J. Am. Chem. Soc.* **2013**, *135* (45), 16833−16836.

(9) Chen, Y.; Li, C. W.; Kanan, M. W. Aqueous CO2 Reduction at Very Low Overpotential on Oxide-Derived Au Nanoparticles. *J. Am. Chem. Soc.* **2012**, *134* (49), 19969−19972.

(10) Li, C. W.; Ciston, J.; Kanan, M. W. Electroreduction of carbon monoxide to liquid fuel on oxide-derived nanocrystalline copper. *Nature* **2014**, *508* (7497), 504−507.

(11) Mistry, H.; Varela, A. S.; Bonifacio, C. S.; Zegkinoglou, I.; Sinev, I.; Choi, Y.-W.; Kisslinger, K.; Stach, E. A.; Yang, J. C.; Strasser, P.; et al. Highly selective plasma-activated copper catalysts for carbon dioxide reduction to ethylene. *Nat. Commun.* **2016**, *7*, 12123.

(12) Liu, M.; Pang, Y.; Zhang, B.; De Luna, P.; Voznyy, O.; Xu, J.; Zheng, X.; Dinh, C. T.; Fan, F.; Cao, C.; et al. Enhanced electrocatalytic CO2 reduction via field-induced reagent concentration. *Nature* **2016**, *537* (7620), 382−386.

(13) Wu, J.; Yadav, R. M.; Liu, M.; Sharma, P. P.; Tiwary, C. S.; Ma, L.; Zou, X.; Zhou, X.-D.; Yakobson, B. I.; Lou, J.; et al. Achieving Highly Efficient, Selective, and Stable CO2 Reduction on Nitrogen-Doped Carbon Nanotubes. *ACS Nano* **2015**, *9* (5), 5364−5371.

(14) Singh, M. R.; Clark, E. L.; Bell, A. T. Effects of electrolyte, catalyst, and membrane composition and operating conditions on the performance of solar-driven electrochemical reduction of carbon dioxide. *Phys. Chem. Chem. Phys.* **2015**, *17* (29), 18924−18936.

(15) Hara, K.; Sakata, T. Large Current Density CO_2 Reduction under High Pressure Using Gas Diffusion Electrodes. *Bull. Chem. Soc. Jpn.* **1997**, *70* (3), 571−576.

(16) Whipple, D. T.; Finke, E. C.; Kenis, P. J. A. Microfluidic Reactor for the Electrochemical Reduction of Carbon Dioxide: The Effect of pH. http://esl.ecsdl.org (accessed Jul 19, 2016).

(17) Hatsukade, T.; Kuhl, K. P.; Cave, E. R.; Abram, D. N.; Jaramillo, T. F. Insights into the electrocatalytic reduction of CO2 on metallic silver surfaces. *Phys. Chem. Chem. Phys.* **2014**, *16* (27), 13814−13819.

(18) Rosen, J.; Hutchings, G. S.; Lu, Q.; Rivera, S.; Zhou, Y.; Vlachos, D. G.; Jiao, F. Mechanistic Insights into the Electrochemical Reduction of CO2 to CO on Nanostructured Ag Surfaces. *ACS Catal.* **2015**, *5* (7), 4293−4299.

(19) Chen, Y.; Lewis, N. S.; Xiang, C. Operational constraints and strategies for systems to effect the sustainable, solar-driven reduction of atmospheric CO2. *Energy Environ. Sci.* **2015**, *8* (12), 3663−3674.

(20) Singh, M. R.; Papadantonakis, K.; Xiang, C.; Lewis, N. S. An electrochemical engineering assessment of the operational conditions and constraints for solar-driven water-splitting systems at near-neutral pH. *Energy Environ. Sci.* **2015**, *8* (9), 2760−2767.

(21) Modestino, M. A.; Hashemi, S. M. H.; Haussener, S. Mass transport aspects of electrochemical solar-hydrogen generation. *Energy Environ. Sci.* **2016**, *9* (5), 1533−1551.

(22) Gupta, N.; Gattrell, M.; MacDougall, B. Calculation for the cathode surface concentrations in the electrochemical reduction of CO2 in KHCO3 solutions. *J. Appl. Electrochem.* **2006**, *36* (2), 161−172.

(23) Horsman, P.; Conway, B. E.; Yeager, E. *Comprehensive Treatise of Electrochemistry: Electrodics: Transport*; Springer Science & Business Media: 2013.

(24) Vogt, H.; Stephan, K. Local microprocesses at gas-evolving electrodes and their influence on mass transfer. *Electrochim. Acta* **2015**, *155*, 348−356.

(25) Janssen, L. J. J. Behaviour of and mass transfer at gas-evolving electrodes. *Electrochim. Acta* **1989**, *34* (2), 161−169.

(26) Gong, X.; Takagi, S.; Matsumoto, Y. The effect of bubble-induced liquid flow on mass transfer in bubble plumes. *Int. J. Multiphase Flow* **2009**, *35* (2), 155−162.

(27) Faber, M. S.; Dziedzic, R.; Lukowski, M. A.; Kaiser, N. S.; Ding, Q.; Jin, S. High-Performance Electrocatalysis Using Metallic Cobalt Pyrite (CoS2) Micro- and Nanostructures. *J. Am. Chem. Soc.* **2014**, *136* (28), 10053−10061.

(28) Yu, C.; Cao, M.; Dong, Z.; Li, K.; Yu, C.; Wang, J.; Jiang, L. Aerophilic Electrode with Cone Shape for Continuous Generation and Efficient Collection of H2 Bubbles. *Adv. Funct. Mater.* **2016**, *26* (37), 6830−6835.

(29) Lu, Z.; Zhu, W.; Yu, X.; Zhang, H.; Li, Y.; Sun, X.; Wang, X.; Wang, H.; Wang, J.; Luo, J.; et al. Ultrahigh Hydrogen Evolution Performance of Under-Water "Superaerophobic" MoS2 Nanostructured Electrodes. *Adv. Mater.* **2014**, *26* (17), 2683−2687.

(30) Li, Y.; Zhang, H.; Xu, T.; Lu, Z.; Wu, X.; Wan, P.; Sun, X.; Jiang, L. Under-Water Superaerophobic Pine-Shaped Pt Nanoarray Electrode for Ultrahigh-Performance Hydrogen Evolution. *Adv. Funct. Mater.* **2015**, *25* (11), 1737−1744.

(31) Kibsgaard, J.; Chen, Z.; Reinecke, B. N.; Jaramillo, T. F. Engineering the surface structure of MoS2 to preferentially expose active edge sites for electrocatalysis. *Nat. Mater.* **2012**, *11* (11), 963−969.

(32) Roušar, I.; Cezner, V. Transfer of mass or heat to an electrode in the region of hydrogen evolution—I theory. *Electrochim. Acta* **1975**, *20* (4), 289−293.

(33) Roušar, I.; Kačin, J.; Lippert, E.; Šmirous, F.; Cezner, V. Transfer of mass or heat to an electrode in the region of hydrogen evolution—II. *Electrochim. Acta* **1975**, *20* (4), 295−299.

(34) Hashiba, H.; Yotsuhashi, S.; Deguchi, M.; Yamada, Y. Systematic Analysis of Electrochemical CO2 Reduction with Various Reaction Parameters using Combinatorial Reactors. *ACS Comb. Sci.* **2016**, *18* (4), 203−208.

(35) Janssen, L. J. J.; Hoogland, J. G. The effect of electrolytically evolved gas bubbles on the thickness of the diffusion layer—II. *Electrochim. Acta* **1973**, *18* (8), 543−550.

(36) Janssen, L. J. J. Mass transfer at gas evolving electrodes. *Electrochim. Acta* **1978**, *23* (2), 81−86.

(37) Eigeldinger, J.; Vogt, H. The bubble coverage of gas-evolving electrodes in a flowing electrolyte. *Electrochim. Acta* **2000**, *45* (27), 4449−4456.

(38) Vogt, H. The actual current density of gas-evolving electrodes—Notes on the bubble coverage. *Electrochim. Acta* **2012**, *78*, 183−187.

(39) Kitagawa, A.; Uchida, K.; Hagiwara, Y. Effects of bubble size on heat transfer enhancement by sub-millimeter bubbles for laminar natural convection along a vertical plate. *Int. J. Heat Fluid Flow* **2009**, *30* (4), 778−788.

(40) Khaselev, O.; Turner, J. A. A Monolithic Photovoltaic-Photoelectrochemical Device for Hydrogen Production via Water Splitting. *Science* **1998**, *280* (5362), 425−427.

(41) Raza, M. Q.; Kumar, N.; Raj, R. Surfactants for Bubble Removal against Buoyancy. *Sci. Rep.* **2016**, *6*, 19113.

(42) Fernández, D.; Maurer, P.; Martine, M.; Coey, J. M. D.; Möbius, M. E. Bubble formation at a gas-evolving microelectrode. *Langmuir* **2014**, *30* (43), 13065−13074.

(43) Kortlever, R.; Shen, J.; Schouten, K. J. P.; Calle-Vallejo, F.; Koper, M. T. M. Catalysts and Reaction Pathways for the Electrochemical Reduction of Carbon Dioxide. *J. Phys. Chem. Lett.* **2015**, *6* (20), 4073−4082.

(44) Tang, W.; Peterson, A. A.; Varela, A. S.; Jovanov, Z. P.; Bech, L.; Durand, W. J.; Dahl, S.; Nørskov, J. K.; Chorkendorff, I. The importance of surface morphology in controlling the selectivity of polycrystalline copper for CO2 electroreduction. *Phys. Chem. Chem. Phys.* **2012**, *14* (1), 76−81.

(45) Nie, X.; Esopi, M. R.; Janik, M. J.; Asthagiri, A. Selectivity of CO2 Reduction on Copper Electrodes: The Role of the Kinetics of Elementary Steps. *Angew. Chem., Int. Ed.* **2013**, *52* (9), 2459−2462.

(46) Li, F.; Zhao, S.-F.; Chen, L.; Khan, A.; MacFarlane, D. R.; Zhang, J. Polyethylenimine promoted electrocatalytic reduction of CO2 to CO in aqueous medium by graphene-supported amorphous molybdenum sulphide. *Energy Environ. Sci.* **2016**, *9* (1), 216−223.

(47) Rosen, J.; Hutchings, G. S.; Lu, Q.; Forest, R. V.; Moore, A.; Jiao, F. Electrodeposited Zn Dendrites with Enhanced CO Selectivity for Electrocatalytic CO2 Reduction. *ACS Catal.* **2015**, *5* (8), 4586−4591.

(48) Kas, R.; Kortlever, R.; Yılmaz, H.; Koper, M. T. M.; Mul, G. Manipulating the Hydrocarbon Selectivity of Copper Nanoparticles in CO2 Electroreduction by Process Conditions. *ChemElectroChem* **2015**, *2* (3), 354−358.

(49) Ren, D.; Deng, Y.; Handoko, A. D.; Chen, C. S.; Malkhandi, S.; Yeo, B. S. Selective Electrochemical Reduction of Carbon Dioxide to Ethylene and Ethanol on Copper(I) Oxide Catalysts. *ACS Catal.* **2015**, *5* (5), 2814−2821.

(50) Schouten, K. J. P.; Pérez Gallent, E.; Koper, M. T. M. The influence of pH on the reduction of CO and to hydrocarbons on copper electrodes. *J. Electroanal. Chem.* **2014**, *716*, 53−57.

(51) Zhang, Y.-J.; Sethuraman, V.; Michalsky, R.; Peterson, A. A. Competition between CO2 Reduction and H2 Evolution on Transition-Metal Electrocatalysts. *ACS Catal.* **2014**, *4* (10), 3742−3748.